Journal of Materials Science & Technology 142 (2023) 76–88

Contents lists available at ScienceDirect

Journal of Materials Science & Technology

journal homepage: www.elsevier.com/locate/jmst

Research Article

Ultra-fast amorphization of crystalline alloys by ultrasonic vibrations

Luyao Li[a,1], Guo-Jian Lyu[b,1], Hongzhen Li[c], Caitao Fan[a], Wenxin Wen[a], Hongji Lin[a], Bo Huang[d], Sajad Sohrabi[a], Shuai Ren[a], Xiong Liang[a], Yun-Jiang Wang[b,e,*], Jiang Ma[a,*], Weihua Wang[f,g]

[a] Guangdong Key Laboratory of Electromagnetic Control and Intelligent Robots, Shenzhen University, Shenzhen 518060, China
[b] State Key Laboratory of Nonlinear Mechanics, Institute of Mechanics, Chinese Academy of Sciences, Beijing 100190, China
[c] National Engineering Research Center of Near-net-shape Forming for Metallic Materials, South China University of Technology, Guangzhou 510640, China
[d] Institute of Materials, School of Materials Science and Engineering, Shanghai University, Shanghai 200444, China
[e] School of Engineering Science, University of Chinese Academy of Sciences, Beijing 101408, China
[f] Songshan Lake Materials Laboratory, Dongguan 523808, China
[g] Institute of Physics, Chinese Academy of Sciences, Beijing 100190, China

ARTICLE INFO

Article history:
Received 27 July 2022
Revised 5 September 2022
Accepted 5 September 2022
Available online 9 November 2022

Keywords:
Amorphization
Ultrasonic vibration
Lattice instability
Elemental diffusion

ABSTRACT

The amorphization of alloys is of both broad scientific interests and engineering significance. Despite considered as an efficient strategy to regulate and even achieve record-breaking properties of metallic materials, a facile and rapid method to trigger solid-state amorphization is still being pursued. Here we report such a method to utilize ultrasonic vibration to trigger amorphization of intermetallic compound. The ultrasonic vibrations can cause tunable amorphization at room temperature and low stress (2 MPa) conveniently. Remarkably, the ultrasonic-induced amorphization could be achieved in 60 s, which is 360 times faster than the ball milling (2.16×10^4 s) with the similar proportion of amorphization. The elements redistribute uniformly and rapidly via the activated short-circuit diffusion. Both experimental evidences and simulations show that the amorphous phase initiates and expands at nanograin boundaries, owing to the induction of lattice instability. This work provides a groundbreaking strategy for developing novel materials with tunable structures and properties.

1. Introduction

As indispensable materials throughout human history, glassy materials play a vital role in optics, biotechnology, medicine and electronics. As a relatively new class of glassy state of matter discovered in 1960s [1], metallic glasses (MGs) possess excellent mechanical properties [2,3], magnetic properties [4,5], high-performance electrocatalysis [6,7], industrial wastewater treatment ability [8,9] as well as great industrial potentials [3,10] due to their unique amorphous structures. As a result, the fabrication of MGs has attracted great interests motivated by both basic curiosity and engineering relevance. Generally, the strategies of amorphization of metallic materials starting from the liquid state [11,12] and vapor state [13], which greatly limits their fundamental scientific understanding and industrial applications [14].

Solid-state amorphization has attracted much attention as a facile fabrication method of MGs without rapid quenching from liquid or gas slates. Since the 1980s, part methods for solid-state amorphization have been reported, such as hydrogenation method [15,16], metal film diffusion coupling method [17,18], radiation-induced method [19,20], ball milling method (mechanical alloying method) [21–24] and deformation-induced method [25,26]. However, these methods are subject to various limitations: excessive time [15,18,24], temperature conditions [15,18], low amorphous contents [18,25] or complex operating conditions [15,19]. The above methods mainly observed two types of amorphization reactions: atomic diffusion at fine scales or lattice disordering induced by defect accumulation. The level of amorphization strongly depends on the concentration and rate of accumulation of lattice defects. Especially for the ball milling, it requires a long defect accumulation time to achieve amorphization, even if it is partial amorphization [24]. Even worse, defect recovery sometimes occurs (affected by shock frequency) in such process [22–24]. Deformation and metal diffusion coupling induced amorphization is difficult over large scale due to that fact that defects usually accumu-

* Corresponding authors.
E-mail addresses: yjwang@imech.ac.cn (Y.-J. Wang), majiang@szu.edu.cn (J. Ma).
[1] These authors contribute equally to this work.

https://doi.org/10.1016/j.jmst.2022.09.028
1005-0302/

late locally [25,27]. As a result, although many solid-state amorphization ways have been reported, a facile and rapid method to trigger solid-state amorphization is still being pursued.

Here we report ultrasonic vibration induced amorphization as a novel approach for the ultra-fast amorphization at room temperature. In this work, the ultrasonic vibrations (20,000 Hz) are utilized to collapse the crystalline structure in intermetallic compounds (IMCs) into an amorphous structure while facilitating the tuning of the amorphous content at room temperature and low stresses (2 MPa) conveniently. The ultrasonic method has an outstanding time advantage (within 60 s) compared to conventional methods, namely the ball milling, hydrogenation and film diffusion coupling method (several hours) [15,18,24]. Ball milling experiments show that the material requires 2.16×10^4 s over the 120 cycles (60 s) of ultrasonic induced amorphization (360 times slower). Meanwhile, the elements are rapidly redistributed uniformly in two-phase crystalline IMC via short-circuit diffusion along the dislocations and grain boundaries (GBs). Both experiments and simulations demonstrate that the amorphization occurs rapidly at the nanocrystalline GBs and then expands at GBs due to the ultra-fast accumulation of defects and induced lattice elastic instability. As a result, the ultrasonic induced amorphization process as a groundbreaking method for developing novel materials with tunable structures and properties. Furthermore, this work provides new insights into the atomic-scale fundamental mechanism of the solid-state amorphization.

2. Experimental procedures

2.1. Preparation of the crystalline IMC

The composition chosen for this work was $Zr_{65}Cu_{17.5}Ni_{10}Al_{7.5}$ (at.%). The MG rods of 2 mm diameter and 100 mm height were first prepared by conventional water-cooled copper mold casting process, followed by micro cutting to cylindrical specimens of 3-mm height and 2-mm diameter. The as-cast MG samples were then heat treated in a vacuum furnace at 820 K ($T>T_x$) for 40 min to achieve a fully crystallized structure. This material was chosen because crystallization of the as-cast MG sample is a convenient way to make two-phase crystalline IMCs.

2.2. Amorphization under ultrasonic vibration

The ultrasonic sonotrode was made of cemented carbide (TC4 titanium alloy) and is combined with a booster and transducer (Fig. 1(b)), which converted the electrical signals into high frequency vibrations (frequency = 20,000 Hz). Therefore, the sonotrode can apply mechanical vibration to the sample under set pressure. In this work, the energy transfer by ultrasonic vibration was controllable and samples were placed in a simple mold (see Fig. S1 in the Supplementary Materials). The crystallized bulk samples were first crushed into small pieces by applying 50 J energy for 0.2 s. After being crushed, the samples were struck with an energy of 100 J for 0.5 s (set for one cycle), and the treatment was repeated for 5, 60 and 120 cycles of ultrasonic vibrations. A considerably shorter interval exists between each cycle to prevent temperature rise. The static force applied during ultrasonic vibration was set to 100 N and the vibration amplitude of sonotrode was 44.4 μm.

The thermal images and corresponding temperature-time profiles were detected by the infrared imaging camera (Fotric 280d) with a macro lens. Load measurement was performed using a self-made dynamometer, and a data-acquisition card (National Instruments NI-9237) with a sampling frequency of 500 Hz was used to transmit the data to a computer. Due to the enclosed environment of the powder beating, its temperature measurement is performed using a homemade thermocouple and a data acquisition card. The high-speed camera was used to capture the crushing process of bulk crystalline IMC, and the video screen playback was slowed down by 160 times compared to reality.

2.3. Ball milling experiment

The ball milling experiments were also carried out on the crystalline IMC in order to compare the ball milling and ultrasonic vibration methods to achieve amorphization. After crushed the bulk raw material into particles, the pre-weighted particles were canned into a high-speed steel vial together with Cr steel balls. A vibratory ball mill with a ball-to-powder ratio of 10:1 and a speed of 200 rpm was used in low vacuum pressure (10^{-3} Pa). The overall ball milling process persisted for 6 h, which was interrupted every 45 min during that. Each interruption was followed by an equal length of time (15 min) to cool down the vials.

2.4. Multi-scale structural characterizations

X-ray diffraction (XRD; Rigaku miniflex600) with CuK_α radiation was used to analyze the structure of the bulk Zr-based MG samples, the crystalline IMC samples and the powder sample obtained by ultrasonic vibration. The scanning electron microscopy (SEM; Fei quanta FEG 450) was used to observe the two-phase distribution of crystalline IMC. The microstructures were characterized by the transmission electron microscopy (TEM, Fei Titan Themis) equipped with energy-dispersive X-ray spectroscopy (EDS). The TEM samples of the crystalline IMC were prepared on FEI Scios SEM/FIB dual beam system. To prepare the TEM sample from the powders, the powders were poured into alcohol and shake for 20 min. The small particle powders were taken in the upper solution and dropped on the molybdenum mesh. The local density of powders after ultrasonic vibration was detected in a room temperature high vacuum cavity with synchrotron radiation energy of 8 keV nano-CT (Beijing Synchrotron Radiation Facility). The size of the structural voxels reconstructed by synchrotron X-ray nano-CT is 64.1 nm$\times$ 64.1 nm $\times$ 64.1 nm, with a spatial resolution of about 100 nm. A 32-bitfloat-type gray value (g) was assigned to each voxel of the reconstructed structure. The gray value of the powder structural image is linearly related to the local absorption coefficient of the sample under test [28], which is positively proportional to the local density of the studied material [29].

2.5. Amorphous content calculation

The amorphous content reflected by XRD results was estimated using a software equipped with the XRD measurement device. Briefly, the calculation is defined by dividing the integrated area of “amorphous peak” by the area of “the sum of amorphous and crystalline peaks”, which is similar to the calculation of crystallinity in Ref. [30]. An example (120 cycled sample) of the calculation method to obtain the amorphous content see Fig. S2 in the Supplementary Materials, in which amorphous and crystalline peaks are obtained by suitable fitting method in software.

2.6. Preparation in MD simulations

MD simulations were performed to reveal the effects of ultrasonic vibrations on the amorphization of the crystalline phases. All the simulations were carried out using the open source LAMMPS package [31]. A Finnis-Sinclair type embedded-atom method (EAM) potential proposed by Mendelev et al. [32] was adopted to describe the atomic interactions. Periodic boundary conditions were applied and the timestep was set 2 fs for all simulations.

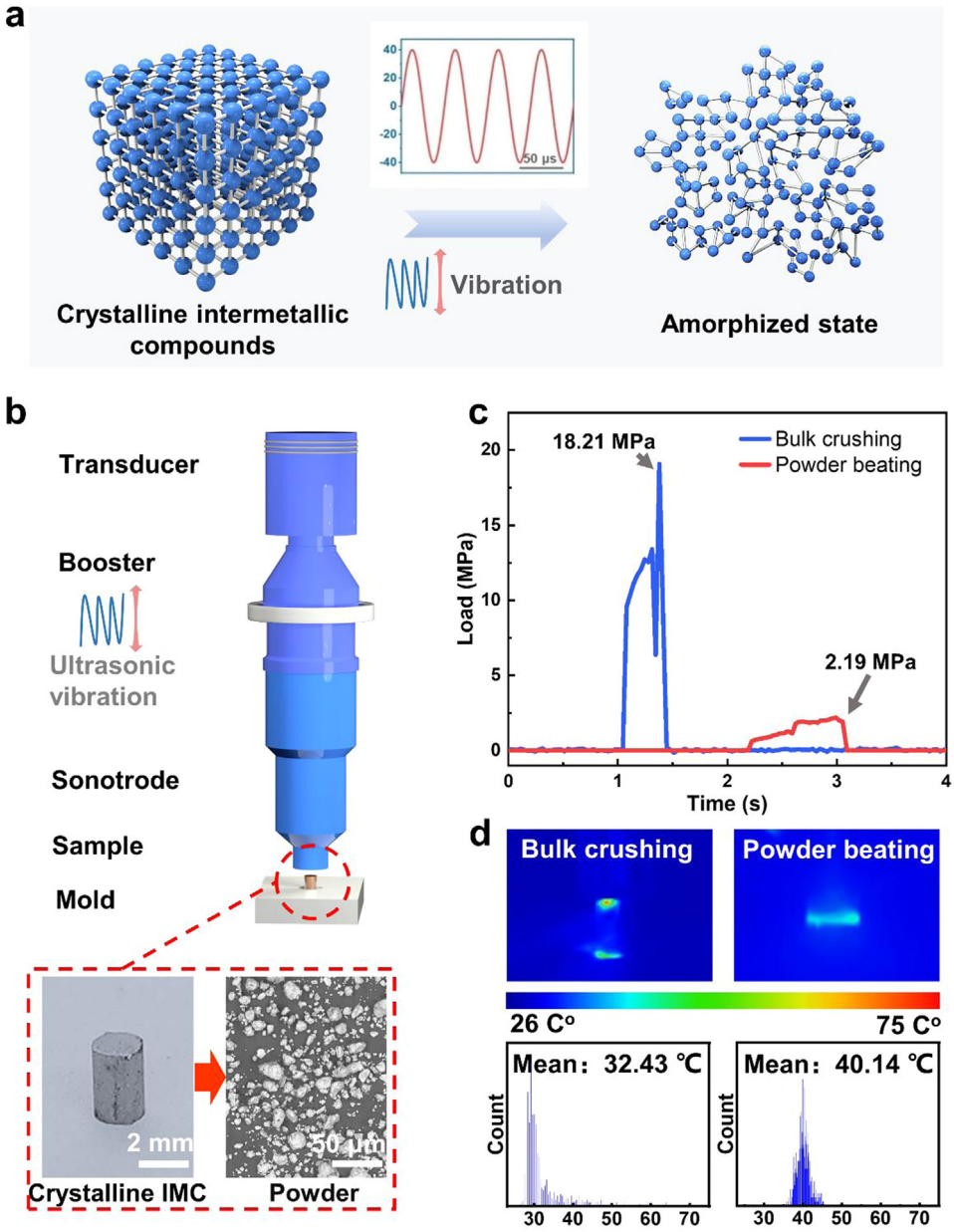

Fig. 1. Schematic diagram of the amorphization process. (a) Illustration of the transformation in atomic structure during the ultrasonic vibration. (b) Schematic of the experimental set-up and the experimental process. The insets show the fabrication of powders from the bulk IMC under ultrasonic vibration. (c) Stress change during the ultrasonic beating of the samples. (d) Temperature analysis of bulk crushing and powder beating under ultrasonic vibration. The upper part shows the thermal image, and the lower part shows the corresponding temperature numerical distribution.

The B2-CuZr polycrystal was constructed using Poisson-Voronoi tessellation method [33–35] with B2-CuZr crystal as the seed of crystalline grain. The polycrystal contains 6 grains and each grain is randomly oriented, with dimensions of 17.9 nm × 17.9 nm × 17.9 nm. To avoid atomic overlaps inside the constructed grain boundary, atoms with distance lower than 2.5 Å were removed. A hydrostatic pressure of 0.5 GPa was then applied for 0.4 ns at 300 K to eliminate the voids near the boundary. After that, the polycrystal was relaxed for another 0.4 ns at zero pressure and 300 K before the high-frequency vibration. For the B2-CuZr inserted glass composite, a $Cu_{50}Zr_{50}$ metallic glass with dimensions of 12.4 nm × 12.4 nm × 12.4 nm was first generated by cooling a well equilibrated liquid from 2000 K to 300 K at 10^{11} K/s, then atoms in a 10 nm-diameter sphere in the center were replaced with B2-CuZr crystal with the same geometry. The [100], [010] and [001] directions of B2-CuZr are set along *x*, *y* and *z* axes, respectively. The composite was then equilibrated at zero pressure and 300 K for 1 ns to obtain a well relaxed glass-crystal interface.

2.7. MD simulations of high-frequency vibration

To mimic the ultrasonic deformation, a uniaxial sinusoidal strain $\varepsilon(t) = \varepsilon_a \sin(2\pi ft)$ was applied on the sample along *Z* axis, where ε_a is the strain amplitude and f is loading frequency, fixed as 10 GHz (thus 100 ps for each cycle) in current simulations. The temperature was fixed at 300 K and the pressure in lateral directions was kept zero during the whole deformation. The atomic configurations were visualized using Ovito software [36]. The deformation on different phases was analyzed by the minimum

of the non-affine squared displacements $D^2_{\min}$, where the non-affine squared displacements $D^2(t,\Delta t)$ is defined as $D^2(t,\Delta t) = \sum_n \sum_i (\vec{r}^i_n(t) - \vec{r}^i_0(t) - \sum_j (\delta_{ij}+\varepsilon_{ij}) \times [\vec{r}^j_n(t-\Delta t) - \vec{r}^j_0(t-\Delta t)])^2$. $D^2_{\min}$ is the local deviation from affine deformation which provides information about non-elastic deformation. The detailed description about $D^2_{\min}$ can be found in Ref. [37].

2.8. Identification of atomic structures

The atomic structures were identified using Polyhedral Template Matching (PTM) method implemented in Ovito software [38]. The PTM algorithm has great reliability in the case of strong thermal fluctuations and strains, thus is suitable for our cases. A reasonable cutoff value of Root-Mean-Square Deviation (RMSD) is required to avoid false identification when using PTM method. The RMSD measures the spatial deviation from standard structure of crystal. The RMSD is defined as $\mathrm{RMSD}(\vec{v},\vec{w}) = \sqrt{\frac{1}{N}\sum_{i=1}^{N} ||\vec{v}_i - \vec{w}_i||^2}$, where $\vec{v}$ contains the position of the central atom and its neighboring atoms and $\vec{w}$ contains those of standard structure templates. Atoms with RMSD greater than the cutoff are identified as the other structure type, while the crystalline structure type with lowest RMSD is eventually assigned to the remaining atoms. In our structural analysis, the cutoff value of RMSD was set to be 0.16.

3. Results and discussion

3.1. Process of amorphization

Schematic diagram of the ultrasonic induced amorphization in Fig. 1(a), illustrates the transformation of the crystalline IMC into an amorphous structure by the utilization ultrasonic vibration. In our previous work, ultrasonic vibration as a special energy transfer mode has been found to open new pathways for the processing and functional application of MGs [39–41]. In the present approach, we have achieved amorphization in the $Zr_{65}Cu_{17.5}Ni_{10}Al_{7.5}$ (at.%) MGs pre annealed to a fully crystallized state having a two phase polycrystalline IMC structure. The ultrasonic vibration experimental apparatus is illustrated in Fig. 1(b). A very low static prepressure (100 N) is applied to the sample by means of an ultrasonic sonotrode for tight compression. Afterwards, the ultrasonic sonotrode is subjected to vibration at a frequency of 20,000 Hz. The vibration shape of the ultrasonic sonotrode was a sinusoidal function with an amplitude of 44.4 μm. The displacement of the ultrasonic sonotrode with respect to time t can be expressed by the equation $d(t) = A\sin(2\pi f \cdot t)$, where A and f denote the amplitude and frequency of the vibration, respectively.

The crystalline bulk IMC can be crushed into particles in just 0.2 s under ultrasonic vibration with an input energy of 50 J and imposed stress of 18.21 MPa (Fig. 1(c)). A high-speed image of the crushing process is shown in Supplementary Video. S1. After the crystalline IMC was completely crushed, the powders were struck with 5, 60 and 120 cycles of ultrasonic vibrations, each cycle being comprised of 100 J input energy for 0.5 s which is equivalent to 10,000 strikes of the sonotrode on the powders. In this stage, the stress of ultrasonic beating is only 2.19 MPa (Fig. 1(c)). It is worth noting that the whole experimental process was achieved at nearly room temperature. To further verify the heat-free mechanism of the ultrasonic process, infrared imaging camera was used to capture the real-time temperature of the sample being processed. The images show that the bulk crystalline IMC samples were crushed at a mean temperature of 32.43 °C and maximum temperature of 66.51 °C. The crushed powders were struck during the ultrasonic vibration process at a mean temperature of 40.14 °C and maximum temperature of 45.30 °C (Fig. 1(d)). In order to further determine the low-temperature properties, the thermocouple was used to measure the temperature when powder beating (see Fig. S3 in the Supplementary Materials), showing that the temperature is close to room temperature (the maximum temperature is 30.5 °C). Also, the low temperature characteristic of ultrasonic treatment can avoid the material contamination by oxygen.

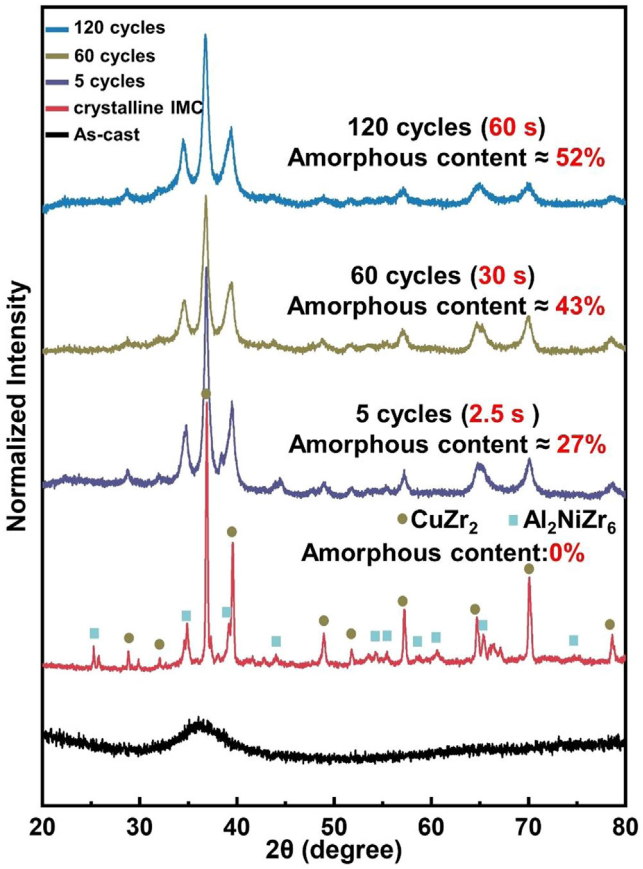

Fig. 2. The X-ray diffraction (XRD) analysis of the as-cast, raw crystalline IMC and powders processed after 5, 60 and 120 cycles. The samples were treated with an energy of 100 J for 0.5 s set for one cycle.

XRD was used to analyze the amorphization process, as shown in Fig. 2. The as-cast bulk MG sample shows a distinct amorphous structure, and the crystalline IMC obtained after the annealing treatment exhibits a large number of crystalline peaks. After analysis it can be determined that the two sets of peaks correspond to $CuZr_2$ and Al_2NiZr_6 crystalline phases. Obviously, as ultrasonic vibration proceeds, the crystalline features gradually weaken as seen from the diffraction peaks of the XRD pattern. Another evidence for the gradually loss of crystal characteristics is that the widths of the crystalline peaks increase substantially as the cycle number of the ultrasonic vibration treatment increases. According to the classical Scherrer formula [42], the increase of the peak broadening indicates decrease in grain size. In this process, large number of low-intensity diffraction peaks even disappear completely, suggesting that the XRD peaks broaden infinitely and the grains disappear. Apart from the grain size effect, the XRD peak broadening may also be caused by other reasons like inhomogeneous strains, twined structure or other point defects that may be present in the crystallites. To reflect the tunability of ultrasonically induced amorphization, we estimated the amorphization content of the struck powders, which are approximately 27%, 43%, and 52% for the 5, 60, and 120 cycles of ultrasonic vibrations, respectively.

3.2. Microstructure characterization of powders

In order to further comprehend the microscopic structure of powders, the transmission electron microscopy (TEM) was used to characterize the morphology and atomic structure during ultrasonic vibration. Fig. 3(a) shows the TEM image of the structures of the crystalline IMC, which consists of two crystalline phases. The microscopic distribution of the two crystalline phases at lower magnifications see Fig. S4 in the Supplementary Materials. In the crystalline IMC, the arrangement of atoms inside the grain is highly ordered and no obvious crystal point or line defects in the sample (Fig. 3(a)), which is in good agreement and more detailed TEM image see Fig. S5 in the Supplementary Materials. To explore the elemental distribution of the crystalline IMC, the energy-dispersive X-ray spectroscopy (EDS) analysis was performed under TEM. The EDS analysis also suggests a two-phase nanocrystalline structure, as shown in Fig. 3(b). By comparing the distribution of each element, it can be understood that the Cu-depleted regions are occupied by the Al and Ni atoms, and this is consistent with the XRD observations in Fig. 2 where Cu-free (Al_2NiZr_6) and Ni/Al-free ($CuZr_2$) phases were detected. The insets in Fig. 3(a) show the specific crystal structures and their Fast Fourier transformation (FFT) images of the selected regions R1 and R2, corresponding to $CuZr_2$ and Al2NiZr$_6$, respectively. By comparing the FFT patterns with the standard XRD features, it is concluded that $CuZr_2$ phase has a BCC structure while Al_2NiZr_6 phase has an HCP structure.

Fig. 3(c) shows the TEM image of the powder treated for 5 cycles of ultrasonic vibrations. The grains of several hundred nanometers in the crystalline IMC are fragmented into massive quantities of ultrafine nanocrystals with different crystallographic orientations, most of them having diameters less than 10 nm. Interestingly, some amorphous layers appear at the boundaries between the neighboring nanocrystals. This observation suggests that the amorphous phase may have emerged from the GBs of the nanocrystals due to the high degree of disorder at the GBs. The more surprising observation is the significant disappearance of the crystal phases in the specimen treated for 60 cycles, as shown in Fig. 3(d). Compared with the sample treated for 5 cycles, the sample struck for 60 cycles exhibits larger fraction of amorphous phase, which leads to a pattern of individual ultrafine nanocrystals surrounded by the amorphous phase. In the specimen treated for 120 cycles, many nanocrystals exhibit even finer dimensions than those observed in the sample struck for 60 cycles, as shown in Fig. 3(e). The insets in Fig. 3(c–e) show the corresponding FFT patterns, which simply reflects the change in the degree of amorphization with the increase in the number of ultrasonic vibration cycles. More TEM images of powders see Fig. S6 in the Supplementary Materials.

The selected area electron diffraction (SAED) ring patterns of the powders after different cycles of ultrasonic vibrations are shown in Fig. 3(f–h). While the observation of the diffusive halo rings in all diffraction patterns reflects the existence of amorphous phase in all processed powders, the progressive disappearance of the polycrystalline rings with the increase in the number of ultrasonic vibration cycles is an indication of achieving larger contents of the amorphous phase. The diffraction pattern of the powders struck for 5 cycles shows multiple polycrystalline rings and a few diffusive halo rings, which indicates the presence of low amorphous phase content and large quantity of nanocrystalline phases having different orientations. Furthermore, in the powders treated for 60 cycles, the massive crystalline phases undergo amorphous phase transitions, which is in line with the observation of brighter diffusive halo ring and duller polycrystalline rings. The polycrystalline rings of the 120-cycled powders have disappeared with only a small amount of the diffraction spots being sparsely distributed, which means that the powder is nearly completely amorphous.

The synchrotron X-ray nano-CT was used to further visualize the powder (around 10 μm) structure. The gray-value images of the powders struck for 60 cycles and 120 cycles (surface and cross section) reconstructed by the nano-CT are shown in Fig. 3(i) and (j). Due to the different absorption of X-rays in different density regions, the region with high gray value (blue region) represents a higher density. It is known that the density of the amorphous state is lower than that of the crystalline state. In the present case, it can be considered that the lower density region (red region) is closer to the amorphous state. The 120-cycled surface exhibits a lower density compared to that of the 60-cycled powder, implying a more amorphous content on the powder surface. The cross sections of the powders were also analyzed, and the results show that the 120-cycled powder already present lower density regions from the edge to the interior, while the 60-cycled sample has relatively high internal density. On the other hand, local high-density regions are still observed inside the 120-cycled powder. The above results demonstrate that the surface of the powder can be amorphized in a relatively short cycle, while longer time is required in the interior area. During the experiments, XRD samples contain massive larger particle powder ($>$ 10 μm) and TEM samples generally with smaller particles (not exceed 1 μm) (Fig. S7 in the Supplementary Materials). During the ultrasonic treatment, the powder was mainly subjected to the action of dry friction, fracture, shearing, etc. under the sonotrode or between the particles, so that the powder surface was subjected to significantly more action than the interior. Due to larger particle powder have a deeper thickness and more difficult to amorphized internally, resulting in a lower amorphous content measured under XRD than TEM. In summary, the amorphous content under XRD represents all powders, while the amorphous content under TEM represents small particle powders.

3.3. Elemental diffusion

The compositional changes of the powders were characterized by the EDS analysis under TEM (Fig. 4). We first observe the as-crushed powder (treated with 50 J energy (0.2 s)) which was processed by the ultrasonic crushing of the crystalline bulk IMC. The EDS results show that the as-crushed powder is chemically heterogenous and the elements have non-uniform distribution (Fig. 4(a)), which is with the EDS results for the crystalline IMC in Fig. 3(b). The non-uniform of element distribution in 5-cycled powders is not as obvious as as-crushed sample (Fig. 4(b)). However, the EDS results for the 120-cycled powder (Fig. 4(d)) demonstrate that the elemental distribution of the powder treated by the ultrasonic vibration is significantly homogeneous. In fact, 60 cycles of ultrasonic vibration will suffice to achieve a nearly homogenous distribution of elements in the powders (Fig. 4(c)).

In order to further observe the uniformity of element distribution in the amorphous and crystalline phases, we performed EDS analysis on 120-cycled powder in a more microscopic area (Fig. 5(a)). The EDS results indicate that not only the elements uniformly distributed in this region, but a sufficient amount of each element is present (Fig. 5(a)). Fig. 5(b) shows the EDS line profiles for the elemental distribution along the crystalline and amorphous phases (the scanning direction shown in Fig. 5(a)). The line profiles do not show significant chemical fluctuations, denoting that there is no compositional distinction in the amorphous and crystalline phases. Thus, it can be inferred from the above facts that the ultrasonic vibrations promote the large-scale transport of the elements and facilitate the elemental homogenization process. Meanwhile, the above results also demonstrate that a polymorphic transition occurred from crystalline to amorphous phase, forming an amorphous phase with a different composition compared to the as-cast MG.

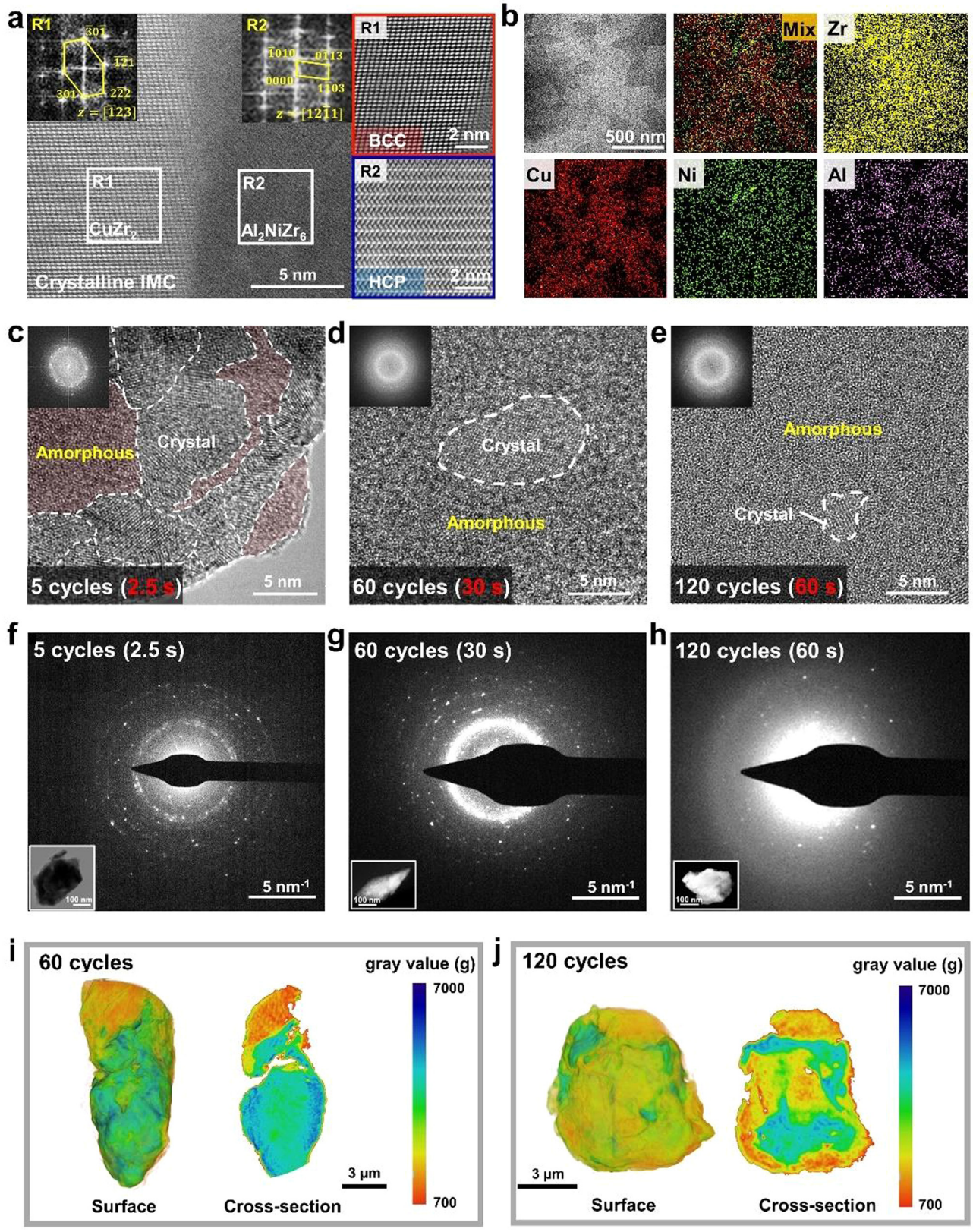

Fig. 3. Microstructure characterization of crystalline and amorphous structures. (a) High-resolution TEM image and structural analysis of the two crystalline phases in the crystalline IMC. The insets show the specific crystal structures and their Fast Fourier transformation (FFT) images of the selected regions R1 and R2 (corresponding to $CuZr_2$ and Al_2NiZr_6 respectively). (b) Energy-dispersive X-ray spectroscopy (EDS) analysis of the crystalline IMC. (c–e) High-resolution TEM images of the powder surface after 5, 60 and 120 cycles of the ultrasonic treatment, respectively. The insets in each panel show the corresponding FFT patterns and the amorphous counted from high-resolution TEM images is shown in the upper right corner. (f–h) SAED ring patterns of the whole powders after 5, 60 and 120 cycles of ultrasonic treatment, respectively. The insets in each panel show the corresponding micro morphologies. (i, j) Synchrotron X-ray nano-CT experiment detecting the microstructure of 60-cycle and 120-cycle powders. The gray-value images (surface and cross section) of the powders clearly show density distribution. Low gray values represent low density (red region).

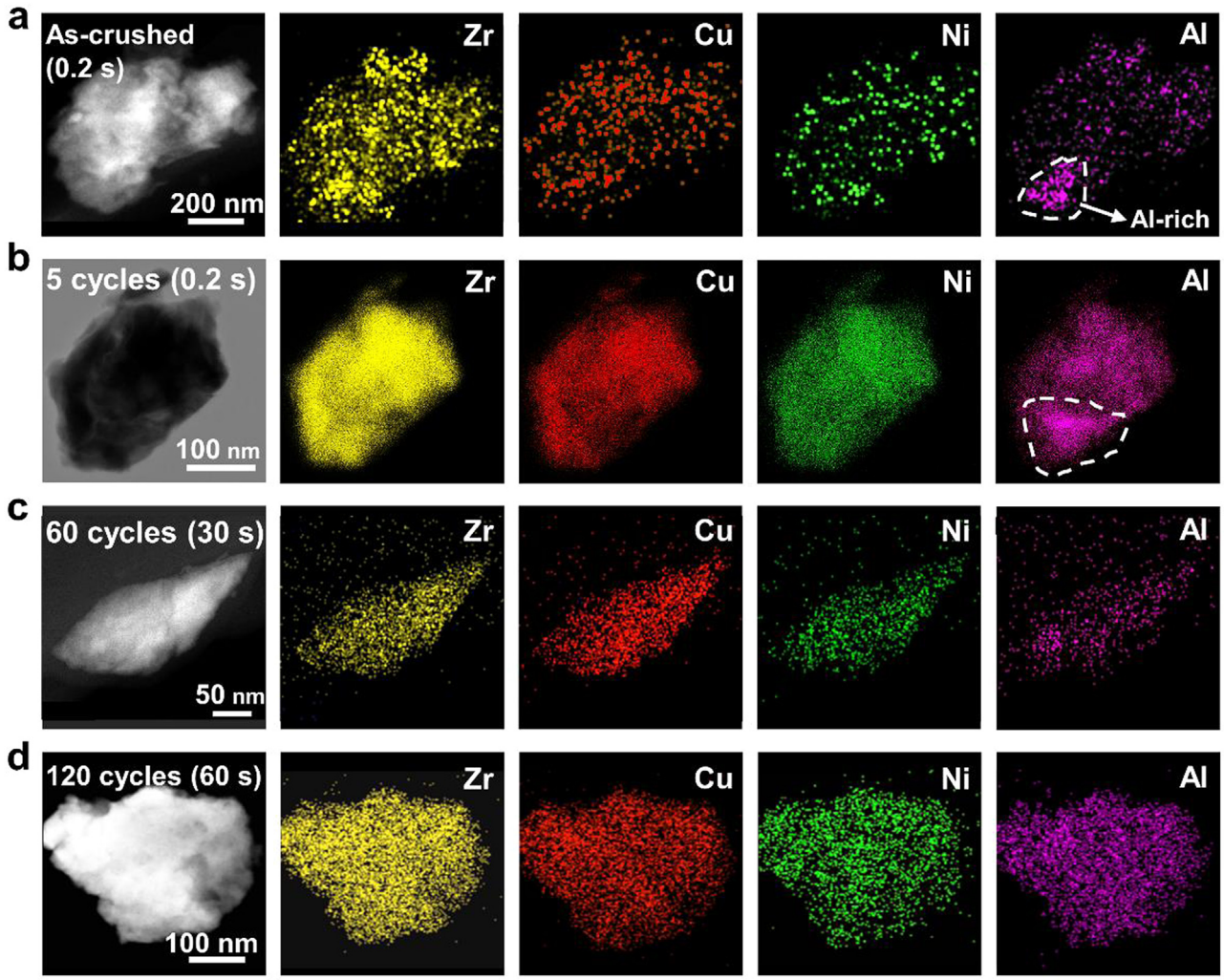

Fig. 4. Elemental homogenization process of powders. (a) as-crushed powder. (b) 5 cycles powder. (c) 60cycles powder. (d) 120 cycles powder.

It is widely accepted that the smaller the solute atom (Al, Ni, Cu), the higher the diffusivity is, which is related to the misfit between the size of the host atom and the solute atom [43]. In addition, owing to the presence of large number of interfaces in the nanocrystals, the diffusion coefficient of nanocrystals is usually several orders of magnitude higher than that in the coarse-grained polycrystals due to the short-circuit GB diffusion mechanism [44]. Moreover, the diffusion coefficient of the high-angle grain boundaries is much higher than that of the low-angle grain boundaries [45,46]. Under ultrasonic vibration, the IMC, which already has a high atomic mismatch, is rapidly grain refined and possesses a high angle GB (Fig. 3(c)). Driven by these factors, the short-circuit (vacancies, dislocations and GBs) diffusions act as the important mechanism of elemental diffusion in the crystal-dominated stages. When the amorphous phase becomes the dominant composition (a period before 60-cycle to 120-cycle), the presence of the amorphous phase would further accelerate the migration of elements due to its thermodynamically metastable state consisting of massive free volume [47,48]. Therefore, apart from local short-circuit diffusion in crystals, diffusion between amorphous phases is extensive in this stage. After going through these processes, complete element homogenization within the particles is achieved.

As for the uniform element distribution of amorphous phase and residual nanocrystalline phase (Fig. 5(a)). It has been previously shown that the diffusing agent can leak from the dislocation pipes into the grain internal, where the grain can absorb elements provided by outside over a period of time [45]. In 120-cycled powder, lots of dislocations in individual nanocrystals (Fig. 5(c)) and disordered atomic arrangement at the boundary (Fig. 5(d)) were found, which continuously absorbed external elements throughout the whole ultrasonic treatment process.

3.4. Advantages of ultrasonic vibration

Fig. 6(a) summarizes the time consumption and amorphous content achieved during various amorphization methods (the detailed list of data points from other amorphization techniques see Table S1. The ultrasonic vibration method not only provides solid-state amorphization at extremely shorter times (several orders of magnitude faster than the other methods), but it also yields a considerable amorphous phase content. To further demonstrate the time advantage of the ultrasonic induction method, ball milling was used to treat the same crystalline IMC sample, as shown in Fig. 6(b). The comparison of XRD results reveal that 2.16×10^4 s of ball milling is required to achieve amorphous phase content almost similar to the one achieved by ultrasonic vibration for 120 cycles (60 s). The above findings highlight the importance of ultrasonic vibration method as a novel amorphization approach, providing a breakthrough strategy for the rapid development of novel materials with tunable structures and properties.

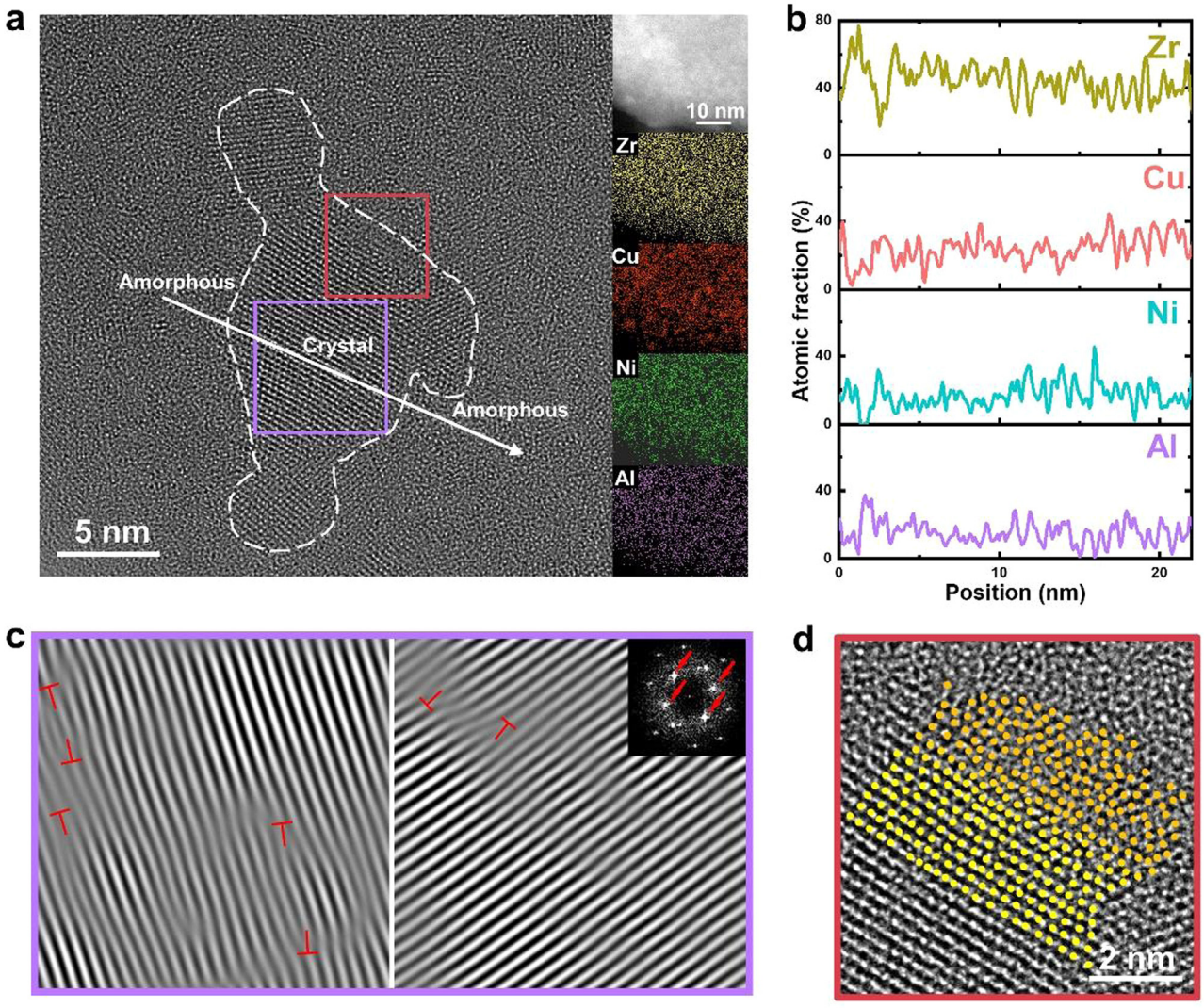

Fig. 5. Crystal-amorphous interface analysis. (a) TEM characterization of the amorphous and crystalline phases in the 120-cycled powder. The insets show the corresponding EDS analysis. (b) The EDS line scanning of the line shown in (a). (c) One-dimensional Fourier-filtered image of the purple area in (a), showing the two highlighted planes in a. Inset is an FFT pattern from the squared area. The four spots (marked by red arrows) in the FFT pattern correspond to two different sets of planes. Dislocations are marked with the symbol ⊥. (d) Atomic arrangement of the red area in (a), which demonstrates the transition from crystalline to amorphous phase.

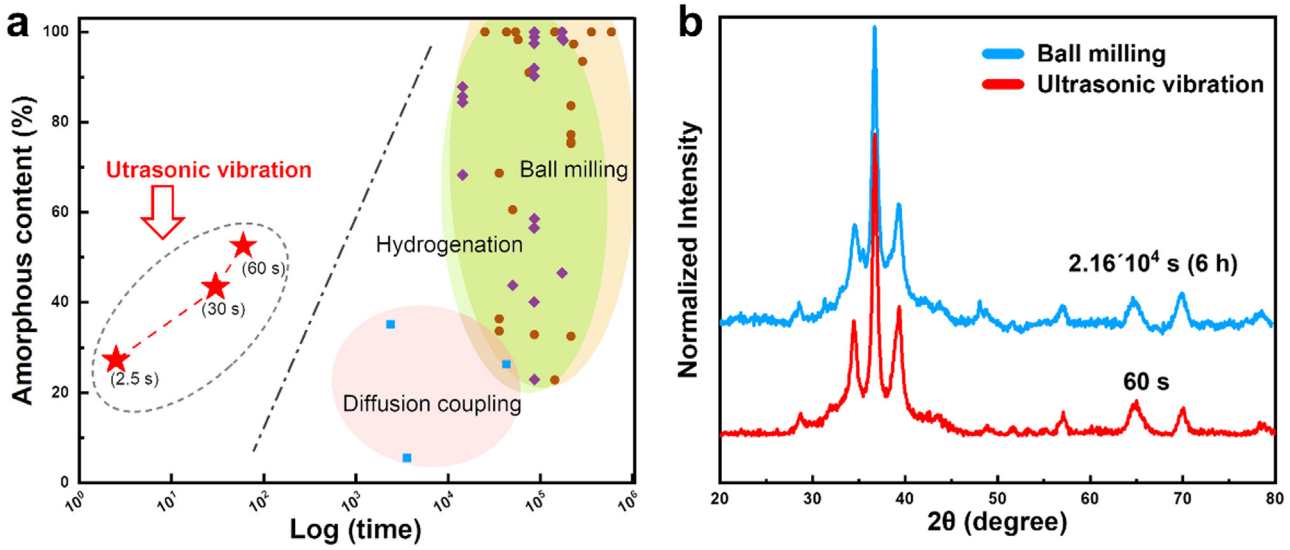

Fig. 6. Comparison of ultrasonic vibration and other methods. (a) Comparison of the time consumption and the amorphous content in various solid-state amorphization methods including ultrasonic vibration. (b) The XRD patterns of the crystalline IMC samples treated with ultrasonic vibration (for 60 s) and ball milling (for 6 h).

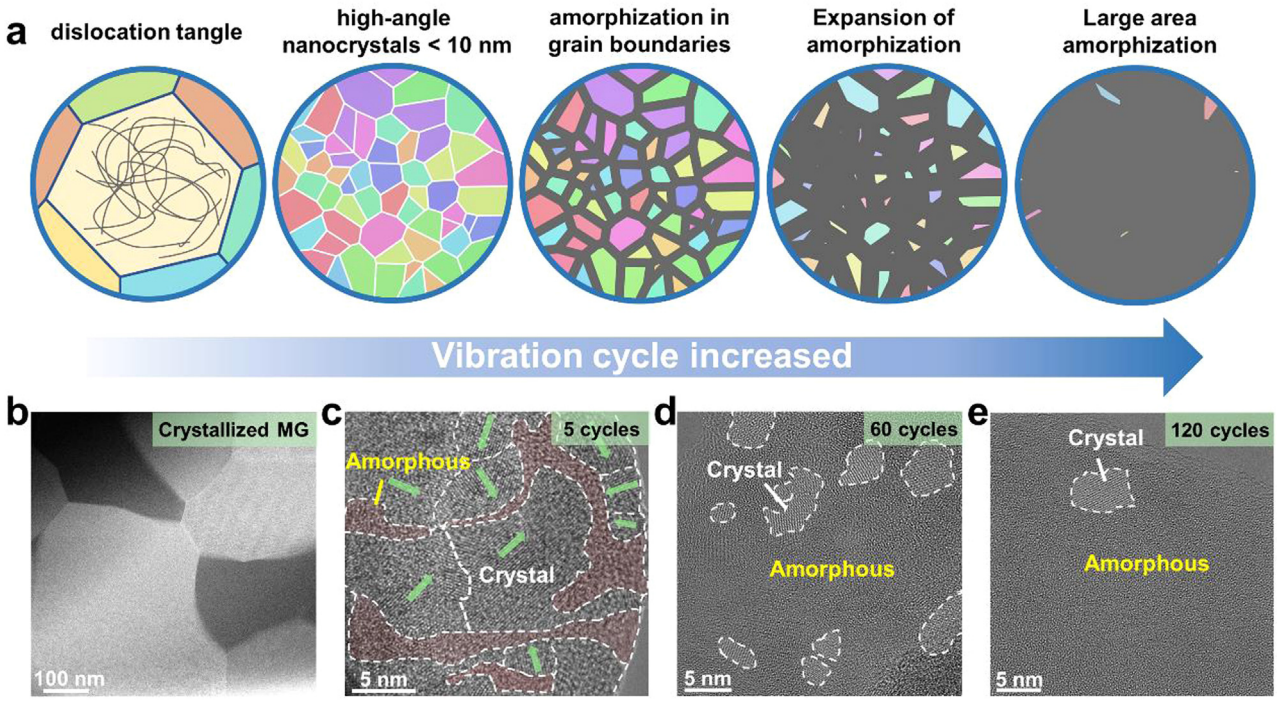

Fig. 7. Schematic diagram of the amorphization mechanism. (a) Schematic diagram illustrating the process of amorphization, in which the change of color means the change of crystal orientation and the black area represents amorphous phase. (b) TEM bright-field image shows the grains of the crystalline IMC (about 500 nm). (c) High-resolution TEM image shows the grain refinement and amorphization initiating at GBs after ultrasonic treatment, and part of the large-angle GBs exists (green arrows represent grain orientation). (d) Gradual reduction of the crystalline phase after amorphization of GBs. (e) Large area amorphization.

3.5. Mechanism of amorphization

The interpretation of the amorphous process can be divided into two stages: (1) the appearance of the amorphous phase; and (2) the expansion of the amorphous phase in the crystalline-amorphous interface.

The ultrasonic vibration makes the crushed powders being subjected not only to the unidirectional cyclic loading but also to the conditions of cold welding, friction, extrusion and fracture, all of which might lead to a successive accumulation of the versatile defects (GBs, dislocations, twins, vacancies, etc.). The schematic diagram of the amorphous process is shown in Fig. 7(a). It is known that the deformation mechanism of the polycrystal with grain sizes in the range of 100–500 nm is similar to that of the conventional fine-grained materials [49] (Fig. 6(b)). The majority of the grains in the bulk crystalline IMC are around 500 nm in size, and at this level the ultrasonic vibrations introduce a high density of dislocations in the sample (see Fig. S8 in the Supplementary Materials). Driven by the ultrasonic energy, these dislocations begin to annihilate, reorganize and aggregate to form dislocation walls and cells [50], which gradually develop into a large number of sub-grains with diameters smaller than 10 nm. With such small grains, deformation in GBs (GB sliding, rotation, and diffusion) become dominant in small sized nanocrystals [51,52]. Under the continuous high-frequency cyclic loading, the orientation of grains becomes large difference such that a large number of the high-angle GBs emerge (Fig. 7(c)). It can be considered that these nanocrystals are the intermediates from crystalline to amorphous phases.

Previous studies have shown that the nanocrystalline state can excite atomic-level strain in the GBs during the solid-state amorphization reactions, consequently triggering mechanical instability in the crystal structure [44]. These GBs, especially the high-angle ones, are usually considered as unstable structures compared to the ordered lattice inside the grains [53]. These instabilities were manifested as movement of lattice atoms from their original positions, triggering significant effects on lattice strain and softening of the elastic modulus [54–56]. In the present work, the high-angle GBs in ultra-fine nanocrystals (Fig. 7(c)) will absorb most of the strain. When the strain under ultrasonic vibration conditions exceeds a threshold value, the crystal structure collapses into the amorphous structure [57,58]. Thus, GBs can be preferentially considered as the origin of nucleation and growth of amorphous phases. This amorphization process can be understood from the TEM results of 5-cycled sample (Fig. 7(c)), which just takes about 2.5 s under ultrasonic vibration.

Fig. 7(d) showed that the size of the crystals surrounded by the amorphous phase is less than 10 nm, which originates from the amorphization of the nanograins initiated from their GBs. Apparently, the gradual expansion of the amorphous phase is mainly driven by the separation of interfacial crystal atoms from the lattice (Fig. 5(d)), which is similar to the amorphization of GBs. After evolving through this process, most of the grains can be completely amorphized (Fig. 7(d) and (e)). Further, the amorphous phase bears most of the strain after extensive amorphization, so the amorphization in crystal-amorphous interface obviously takes longer time (60 s for 120-cycled sample).

3.6. Atomic origin of the amorphization under ultrasonic vibration

The MD simulations were performed to further reveal the atomic mechanism of the amorphization of the crystalline phases under high-frequency vibrations. Two representative model systems, B2-CuZr polycrystal and spherical B2-CuZr inserted $Cu_{50}Zr_{50}$ glass composite, were chosen to investigate the initiation and evolution of amorphization, respectively. Fig. 8 represents the structural evolution of the B2-CuZr polycrystal during a 10 ns high-frequency vibration at 300 K. The applied strain and the resulting stress are shown in Fig. 8(a, b) as a function of time. The maximum strain amplitude ε_a is set as 6% (within the marginal elastic regime), which is not too large to destroy the sample imme-

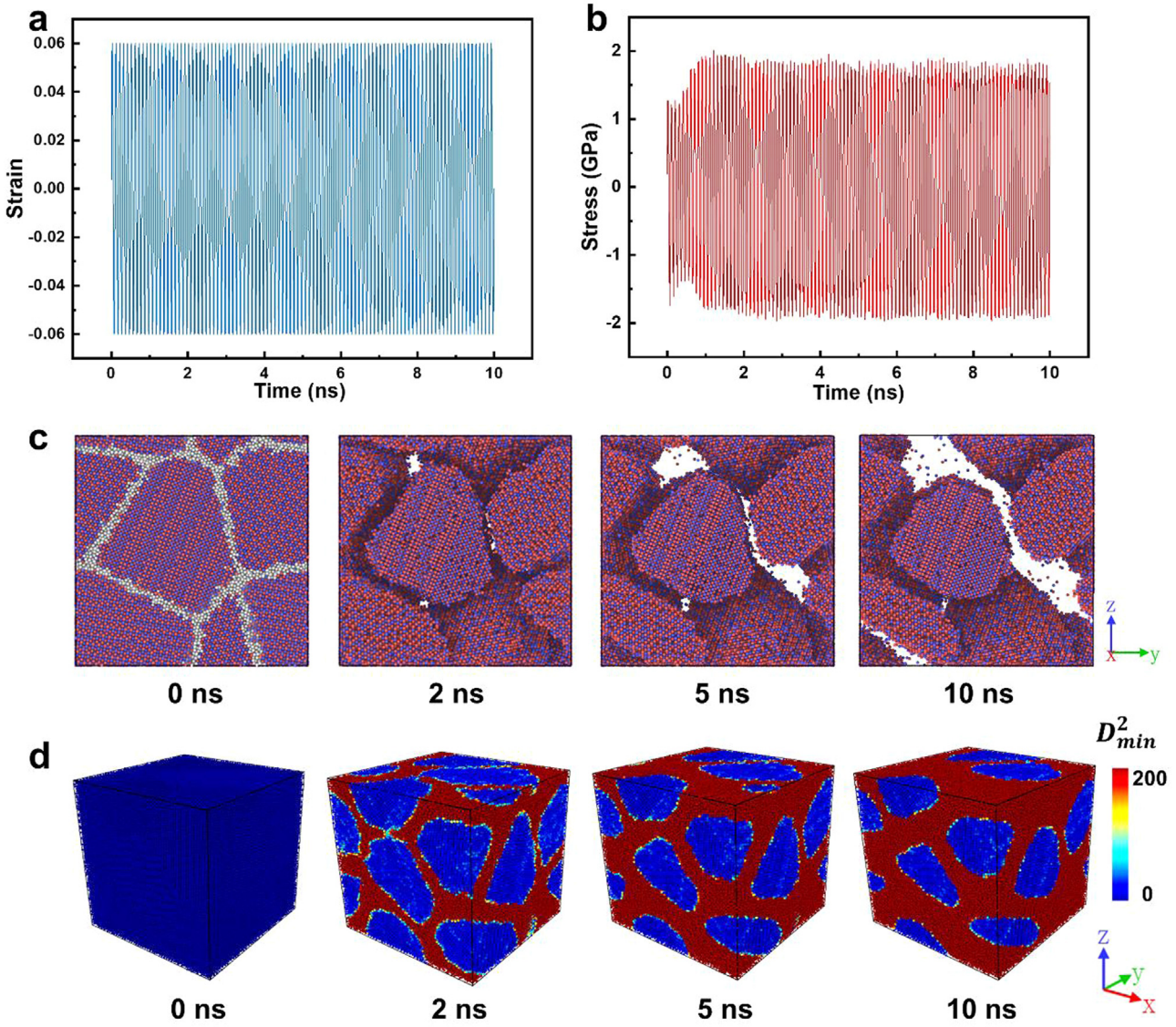

Fig. 8. Evolution of the B2-CuZr polycrystal at the initial stage of amorphization during high-frequency vibration in at 300 K. (a) The cyclic deformation protocol in MD simulation illustrated by the time-dependent applied strain. (b) Resulting stress under ultrasonic vibration with strain amplitude of $\varepsilon_a = 6\%$. (c) Structural evolution of the B2-CuZr polycrystal with amorphous regions (atoms identified as the other structure type) removed. (d) Non-affine squared displacement $D^2_{\min}$ coloring of the B2-CuZr polycrystal during the vibration.

diately meanwhile not too small to prevent the sample from being elastically deformed during the whole simulation process. As shown in Fig. 8(c), it can be clearly observed that the size of each grain gradually decreases under the vibration, which confirms that the amorphization starts from the GBs as we have observed in experiments. This scenario is quite different from the grain growth mechanism under thermal condition. Furthermore, Fig. 8(d) represents the minimum of the non-affine squared displacement $D^2_{\min}$ (see Experimental procedures) of the corresponding configurations. A marked separation between crystalline and amorphous regions is visible. It can be inferred that under vibration the GBs are more vulnerable than the grains, therefore, the amorphization originates from GBs at the initial stage. With the gradual expansion of the amorphous region, most of the deformation will localize in the amorphous region, while the grain interior will be deformed elastically.

Once the GBs transformed into amorphous phase at the initial stage, the original B2-CuZr polycrystal can be treated as a composite containing the B2-CuZr and the glass matrix. To better investigate the progress-end stage of amorphization, a spherical B2-CuZr inserted glass composite was designed and cyclically deformed with the same magnitude of strain (Fig. 9). Fig. 9(a) shows a slice of the composite before loading, where a spherical B2-CuZr crystal is embedded in a $Cu_{50}Zr_{50}$ glass matrix. Fig. 9(b) shows the histogram of RMSD (see Experimental procedures) during the vibration. The RMSD values of crystalline and amorphous atoms clearly separate throughout the entire amorphization process, thus a cut-off value of 0.16 was chosen for the structural identification. The amorphization of the spherical B2-CuZr crystal with the loading time under the vibration is presented in Fig. 9(c). For better visualization of the amorphization process, the original glass matrix was removed during the vibration. As seen, atoms gradually depart from the surface of B2-CuZr crystal, and more and more atoms diffuse from the surface into the glass matrix until complete transformation to amorphous. Moreover, the atomic diffusion in the loading direction is significantly faster than other directions, resulting in the remaining B2-CuZr crystal appearing ellipsoidal. In our experiments, we noticed that amorphization starts quickly at the be-

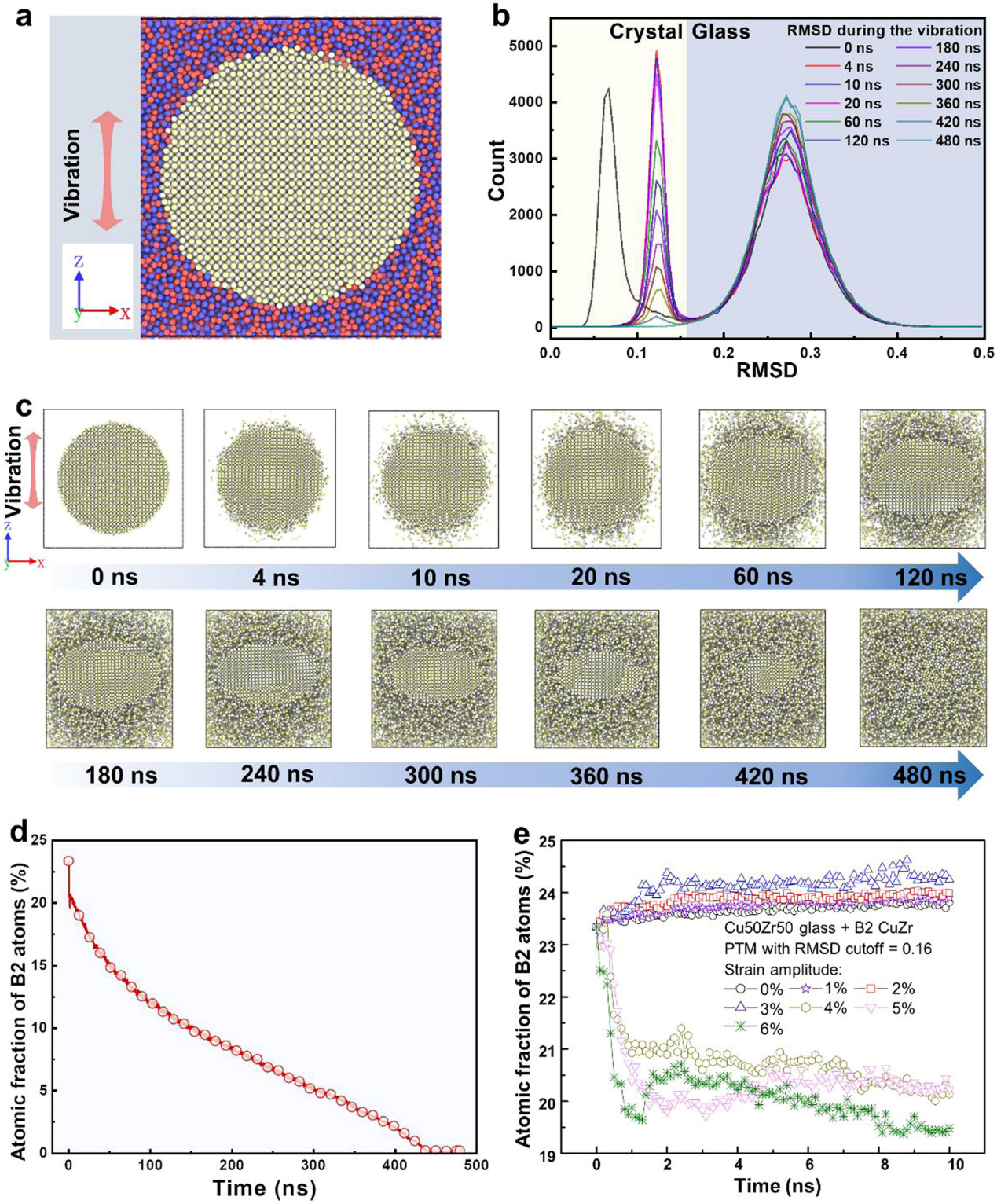

Fig. 9. Evolution of the B2-CuZr inserted glass composite at the progress-end stage of amorphization during high-frequency vibration at 300 K. (a) A slice of atomic configuration of the composite before the vibration, with Cu and Zr atoms colored red and blue in the glass matrix while yellow and white in B2-CuZr, respectively. (b) Histogram of RMSD at different time of the vibration in 6% strain amplitude, with 100 bins ranging from 0 to 0.5 Å. (c) The process of amorphization of the inserted B2-CuZr. (d) Fraction of the atoms in B2 crystalline phase during the vibration. (e) Time dependence of atomic fraction of B2 atoms under different strain amplitudes.

ginning and then slows down. It requires only 5 cycles to start amorphization, while it takes 120 cycles to be nearly fully amorphized (Fig. 7(c–e)). Fig. 9(d) shows the time dependence of B2 fraction. The amorphization rate gradually decreases as the loading continues, which is consistent with the observation in experiment.

The process of amorphization under high-frequency vibration is dependent on strain amplitude, since atomic mobility increases significantly with the increase of strain magnitude. To reveal the effect of strain amplitude, we also conducted vibrations with various strain amplitudes on the B2-CuZr inserted glass composite

(see Figs. S9 and S10). With lower strain amplitudes (1%–3%), the atomic fraction of crystal slowly increases, corresponding to the process of crystallization. By contrast, higher strain amplitudes (4%–6%) result in amorphization (see Fig. 9(e)). As well known, higher temperatures promote atomic mobility. For a crystalline alloy, temperatures lower than melting point leads to crystallization, while higher than melting point leads to melting. In our simulations, the temperature was always fixed at 300 K. Therefore, it is inferred that the high-frequency vibration has similar effects as temperature: both can promote the atomic mobility. Moreover, large strain amplitude or high temperature easily leads to amorphization (or melting). The two scenarios represent either mechanically driven or thermally activated lattice instability of crystalline lattice.

4. Summary

In summary, we propose an ultra-fast and easy-to-operate strategy to induce amorphization of crystalline by ultrasonic vibrations under near room temperature and low-stress conditions. In the early stages of ultrasonic vibration, the defect concentration inside the sample increases dramatically involving critical role of grain boundary dynamics. When the grains are quite small (<10 nm), the GBs bear most of the strain in the form of lattice atomic displacements, triggering elastic instability and then achieving amorphization. As the vibration cycle increases, these amorphous phases initiated at GBs continue to expand into the grain interiors and eventually yield large fraction of amorphization. In this process, the elements (Al, Ni, and Cu) inside the two-phase crystalline IMC diffuse through short-circuit channels (e.g., dislocations and grain boundaries), which homogenizes the elements inside the individual powder. All the above processes happen in a very short period of time (within 60 s). The atomistic mechanism of amorphization starting from GBs and with significant role of mass transport from GBs to interior has been captured by molecular dynamics simulations. Based on the current approach, ultrasonic vibrations may enable fast amorphization of new materials which sounds implausible by implementing the conventional solid-state amorphization methods. Meanwhile, this work provides a new observation window to trace the fundamental mechanism of order-disorder transition down to the atomic scale.

Declaration of Competing Interest

The authors declare that they have no known competing financial interests or personal relationships that could have appeared to influence the work reported in this paper.

CRediT authorship contribution statement

Luyao Li: Investigation, Formal analysis, Writing – original draft. **Guo-Jian Lyu:** Investigation, Formal analysis. **Caitao Fan:** Investigation, Formal analysis. **Wenxin Wen:** Investigation, Formal analysis. **Hongji Lin:** Investigation, Formal analysis. **Bo Huang:** Investigation, Formal analysis. **Sajad Sohrabi:** Writing – review & editing. **Shuai Ren:** Writing – review & editing. **Xiong Liang:** Writing – review & editing. **Yun-Jiang Wang:** Supervision, Resources, Writing – review & editing. **Jiang Ma:** Supervision, Resources, Writing – review & editing. **Weihua Wang:** Supervision, Resources.

Acknowledgments

The work was financially supported by the Key Basic and Applied Research Program of Guangdong Province, China (No. 2019B030302010), the National Natural Science Foundation of China (Nos. 52122105, 51971150, 51871157), the National Key Research and Development Program of China (No. 2018YFA0703605). Y.J.W. acknowledges the financial support from the National Natural Science Foundation of China (No. 12072344), and the Youth Innovation Promotion Association of the Chinese Academy of Sciences. The numerical calculations were performed on the CAS Xiandao-1 computing environment. This research was supported by the Beijing Electron Positron Collider (BEPC) project (No. 2020-BEPC-PT-004661). The authors thank the assistance on microscope observation received from the Electron Microscope Center of the Shenzhen University.

Supplementary materials

Supplementary material associated with this article can be found, in the online version, at doi:10.1016/j.jmst.2022.09.028.

References

[1] W. Klement, R. Willens, P. Duwez, Nature 187 (1960) 869–870.
[2] J. Pan, Y.P. Ivanov, W. Zhou, Y. Li, A. Greer, Nature 578 (2020) 559–562.
[3] C.A. Schuh, T.C. Hufnagel, U. Ramamurty, Acta Mater. 55 (2007) 4067–4109.
[4] M. Stoica, R. Li, A.R. Yavari, G. Vaughan, J. Eckert, N. Van Steenberge, D.R. Romera, J. Alloys Compd. 504 (2010) S123–S128.
[5] T. Itoi, T. Takamizawa, Y. Kawamura, A. Inoue, Scr. Mater. 45 (2001) 1131–1137.
[6] Y. Yan, C. Wang, Z. Huang, J. Fu, Z. Lin, X. Zhang, J. Ma, J. Shen, J. Mater. Chem. A 9 (2021) 5415–5424.
[7] Z.J. Wang, M.X. Li, J.H. Yu, X.B. Ge, Y.H. Liu, W.H. Wang, Adv. Mater. 32 (2020) 1906384.
[8] L. Zhang, L. Qiu, Q. Zhu, X. Liang, J. Huang, M. Yang, Z. Zhang, J. Ma, J. Shen, Appl. Catal. B-Environ. 294 (2021) 120258.
[9] Z. Jia, Q. Wang, L. Sun, Q. Wang, L.C. Zhang, G. Wu, J.H. Luan, Z.B. Jiao, A. Wang, S.X. Liang, Adv. Funct. Mater. 29 (2019) 1807857.
[10] L.-C. Zhang, Z. Jia, F. Lyu, S.-X. Liang, J. Lu, Prog. Mater. Sci. 105 (2019) 100576.
[11] A. Inoue, Acta Mater. 48 (2000) 279–306.
[12] W.-H. Wang, C. Dong, C. Shek, Mater. Sci. Eng. R 44 (2004) 45–89.
[13] P. Luo, C. Cao, F. Zhu, Y. Lv, Y. Liu, P. Wen, H. Bai, G. Vaughan, M. Di Michiel, B. Ruta, Nat. Commun. 9 (2018) 1389.
[14] W.L. Johnson, G. Kaltenboeck, M.D. Demetriou, J.P. Schramm, X. Liu, K. Samwer, C.P. Kim, D.C. Hofmann, Science 332 (2011) 828–833.
[15] K. Aoki, X. Li, T. Masumoto, Acta Metall. Mater. 40 (1992) 1717–1726.
[16] K. Aoki, T. Yamamoto, Y. Satoh, K. Fukamichi, T. Masumoto, Acta. Metall. 35 (1987) 2465–2470.
[17] L. Chen, Mater. Sci. Eng. R 29 (2000) 115–152.
[18] E.J. Cotts, W. Meng, W. Johnson, Phys. Rev. Lett. 57 (1986) 2295.
[19] B. Liu, W. Lai, Q. Zhang, Mater. Sci. Eng. R 29 (2000) 1–48.
[20] R.C. Ewing, A. Meldrum, L. Wang, S. Wang, Rev. Mineral. Geochem. 39 (2000) 319–361.
[21] M.S. El-Eskandarany, J. Saida, A. Inoue, Acta Mater. 50 (2002) 2725–2736.
[22] B. Murty, M.M. Rao, S. Ranganathan, Acta Metall. Mater. 43 (1995) 2443–2450.
[23] R. Schwarz, R. Petrich, J. Less. Common. Met. 140 (1988) 171–184.
[24] Y. Chen, M. Bibole, R.Le Hazif, G. Martin, Phys. Rev. B 48 (1993) 14.
[25] S. Zhao, Z. Li, C. Zhu, W. Yang, Z. Zhang, D.E. Armstrong, P.S. Grant, R.O. Ritchie, M.A. Meyers, Sci. Adv. 7 (2021) eabb3108.
[26] H. Wang, D. Chen, X. An, Y. Zhang, S. Sun, Y. Tian, Z. Zhang, A. Wang, J. Liu, M. Song, Sci. Adv. 7 (2021) eabe3105.
[27] J. Cheng, L. Chen, J. Appl. Phys. 68 (1990) 4002–4007.
[28] B. Huang, T. Ge, G. Liu, J. Luan, Q. He, Q. Yuan, W. Huang, K. Zhang, H. Bai, C. Shek, Acta Mater. 155 (2018) 69–79.
[29] L. Lindgren, Wood Sci. Technol. 25 (1991) 341–349.
[30] P. Wesseling, B. Ko, J.J. Lewandowski, Scr. Mater. 48 (2003) 1537–1541.
[31] S. Plimpton, J. Comput. Phys. 117 (1995) 1–19.
[32] M. Mendelev, Y. Sun, F. Zhang, C.-Z. Wang, K.-M. Ho, J. Chem. Phys. 151 (2019) 214502.
[33] W. Brostow, J.-P. Dussault, B.L. Fox, J. Comput. Phys. 29 (1978) 81–92.
[34] J.L. Finney, J. Comput. Phys. 32 (1979) 137–143.
[35] P. Hirel, Comput. Phys. Commun. 197 (2015) 212–219.
[36] A. Stukowski, Model. Simul. Mater. Sci. Eng. 18 (2009) 015012.
[37] M.L. Falk, J.S. Langer, Phys. Rev. E 57 (1998) 7192.
[38] P.M. Larsen, S. Schmidt, J. Schiøtz, Model. Simul. Mater. Sci. Eng. 24 (2016) 055007.
[39] J. Ma, C. Yang, X.D. Liu, B.S. Shang, Q.F. He, F.C. Li, T.Y. Wang, D. Wei, X. Liang, X.Y. Wu, Y.J. Wang, F. Gong, P.F. Guan, W.H. Wang, Y. Yang, Sci. Adv. 5 (2019) eaax7256.
[40] X. Li, X. Liang, Z. Zhang, J. Ma, J. Shen, Scr. Mater. 185 (2020) 100–104.
[41] Z. Huang, J. Fu, X. Li, W. Wen, H. Lin, Y. Lou, F. Luo, Z. Zhang, X. Liang, J. Ma, Sci. China Mater. 65 (2022) 255–262.
[42] A. Patterson, Phys. Rev. 56 (1939) 978.
[43] H. Hahn, R. Averback, Phys. Rev. B 37 (1988) 6533.
[44] D. Sundararaman, Mater. Sci. Eng. B 32 (1995) 307–313.
[45] L. Klinger, E. Rabkin, Interface Sci. 6 (1998) 197–203.

[46] X. Li, Y. Chou, Acta Mater. 44 (1996) 3535–3541.
[47] K. Rätzke, P. Hüppe, F. Faupel, Phys. Rev. Lett. 68 (1992) 2347.
[48] M. Sun, A. Rauf, Y. Zhang, G. Sha, G. Peng, Z. Yu, C. Guo, Y. Fang, S. Lan, T. Feng, Mater. Res. Lett. 6 (2018) 55–60.
[49] F. Dalla Torre, P. Spätig, R. Schäublin, M. Victoria, Acta Mater. 53 (2005) 2337–2349.
[50] Z. Li, X. Li, Z. Huang, Z. Zhang, X. Liang, H. Liu, P.K. Liaw, J. Ma, J. Shen, Acta Mater. 225 (2022) 117569.
[51] H. Van Swygenhoven, Science 296 (2002) 66–67.
[52] T. Rupert, D. Gianola, Y. Gan, K. Hemker, Science 326 (2009) 1686–1690.
[53] M.A. Meyers, A. Mishra, D.J. Benson, Prog. Mater. Sci. 51 (2006) 427–556.
[54] G. Lopez-Polin, C. Gomez-Navarro, V. Parente, F. Guinea, M.I. Katsnelson, F. Perez-Murano, J. Gomez-Herrero, Nat. Phys. 11 (2015) 26–31.
[55] F. Gao, W.J. Weber, Phys. Rev. B 69 (2004) 224108.
[56] J. Dong, Y. Huan, B. Huang, J. Yi, Y. Liu, B. Sun, W. Wang, H. Bai, Innovation 2 (2021) 100106.
[57] E. Ma, Scr. Mater. 49 (2003) 941–946.
[58] J. Koike, Phys. Rev. B 47 (1993) 7700.